

# PCCP

Accepted Manuscript

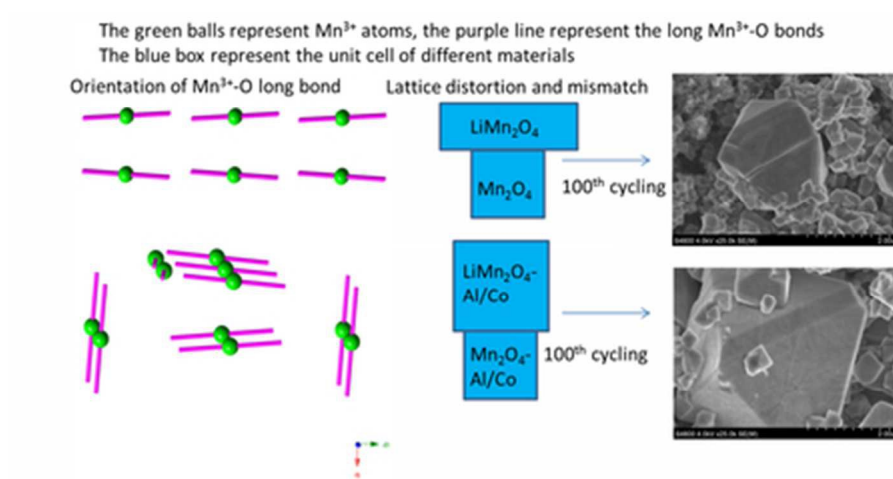


This is an *Accepted Manuscript*, which has been through the Royal Society of Chemistry peer review process and has been accepted for publication.

*Accepted Manuscripts* are published online shortly after acceptance, before technical editing, formatting and proof reading. Using this free service, authors can make their results available to the community, in citable form, before we publish the edited article. We will replace this *Accepted Manuscript* with the edited and formatted *Advance Article* as soon as it is available.

You can find more information about *Accepted Manuscripts* in the [Information for Authors](#).

Please note that technical editing may introduce minor changes to the text and/or graphics, which may alter content. The journal's standard [Terms & Conditions](#) and the [Ethical guidelines](#) still apply. In no event shall the Royal Society of Chemistry be held responsible for any errors or omissions in this *Accepted Manuscript* or any consequences arising from the use of any information it contains.



39x19mm (300 x 300 DPI)



## ARTICLE

## Dual-doping to suppress cracking in spinel $\text{LiMn}_2\text{O}_4$ : a joint theoretical and experimental study

Received 00th January 20xx,  
Accepted 00th January 20xx

DOI: 10.1039/x0xx00000x

www.rsc.org/

Zhifeng Zhang<sup>a</sup>, Zhenlian Chen<sup>a\*</sup>, Guangjin Wang<sup>a,b</sup>, Heng Ren<sup>a</sup>, Mu Pan<sup>b</sup>, Lingli Xiao<sup>c</sup>, Kuicheng Wu<sup>c</sup>, Liutao Zhao<sup>c</sup>, Jianqing Yang<sup>c</sup>, Qingguo Wu<sup>c</sup>, Jie Shu<sup>d</sup>, Dongjie Wang<sup>d</sup>, Hongli Zhang<sup>e</sup>, Ni Hud<sup>f</sup>, Jun Li<sup>a\*</sup>

**Abstract** Electrochemical cycling stabilities were compared for undoped and Al/Co dual-doped spinel  $\text{LiMn}_2\text{O}_4$  synthesized by solid state reactions. We observed the suppression of particle fracture in Al/Co dual-doped  $\text{LiMn}_2\text{O}_4$  during charging/discharging cycling and its distinguishable particle morphology with respect to undoped material. Systematic first-principles calculations were performed on undoped, Al or Co single-doped, and Al/Co dual-doped  $\text{LiMn}_2\text{O}_4$  to address their structural differences at the atomistic level. We reveal that while Jahn-Teller distortion associating with  $\text{Mn}^{3+}\text{O}_6$  octahedron is the origin of the lattice strain, the networking, i.e., the distribution of mixing valence Mn ions is much more important to release the lattice strain, then to alleviate particle cracking. The calculation showed that the lattice mismatching between  $\text{Li}^+$  intercalation and deintercalation of  $\text{LiMn}_2\text{O}_4$  can be significantly reduced by dual-doping, and then the volumetric shrinkage during delithiation. This may account for the nearly disappearance of cracks on the surface of Al/Co- $\text{LiMn}_2\text{O}_4$  after 350 cycles, while some obvious cracks have developed in undoped  $\text{LiMn}_2\text{O}_4$  at similar particle size even after 50 cycles. In turn, Al/Co dual-doped  $\text{LiMn}_2\text{O}_4$  showed a good cycling stability with capacity retention rate 84.1% after 350 cycles at the rate of 1C, 8% higher than undoped phase.

### 1 Introduction

Pulverization in cathode or anode materials is a major material deficiency that strongly impacts on electrochemical performance of lithium-ion battery (LIB). Cracks may develop on particle surface during cycling, leading to battery degradation in cellphone or laptop uses, and hinder LIB applications to electric transportation and power grid.<sup>1-3</sup> They occur not only in large particles at micron size but also in materials on nanoscale. Teki and Pu et al. have observed cracks in anodes Si and Sn particles of about 150nm.<sup>4,5</sup> Deyu Wang and Haifeng Wang et al. have found cathodes  $\text{LiFePO}_4$  and  $\text{LiCoO}_2$  particles of 500nm could generate cracks within 50 cycles.<sup>6,7</sup> It is widely believed that cracking is much more inclining to occur in large particles of microns. Spinel  $\text{LiMn}_2\text{O}_4$  may suffer particle fracture even in the first delithiation process when particle size is about  $3\mu\text{m}$ .<sup>8</sup> The cracking mechanism has been generally attributed to the large lattice strain when a particle changes volume significantly during charge and discharge cycling. However, the physical connection between lattice distortion and local bonding characteristic has rarely addressed in literature. That is often material dependent. Therefore, it is difficult to decipher a common

physical root of lattice strains, this hinders the development of efficient solutions to stall or inhibit particle cracking in electrochemical cycling.

Lithium spinel  $\text{LiMn}_2\text{O}_4$  (LMO) has found application in all-electric vehicles due to its safety, low cost, non-toxicity and abundance of Mn in earth's crust. Extensive studies have been executed to improve its long-term cycling performance by optimizing crystal structure. Conventionally, cubic  $Fd\bar{3}m$  symmetry is assigned to LMO with Li ions occupying tetrahedral 8a sites, and Mn ions on 16d octahedral sites. However, structure transition was observed around room temperature,<sup>9-12</sup> and neutron diffraction spectra at low temperature suggested very complicated supercell relating to the charge ordering, i.e., the distribution pattern of mixing valences  $\text{Mn}^{3+}$  and  $\text{Mn}^{4+}$ .<sup>13</sup> Tri-valence Mn is a typical ion relating to Jahn-Teller distortion and plays a key role in lithium chemistry of LMO as the active redox centre, determining reversible capacity of LMO. Although the previous experiments have attributed the structure transition with lattice distortion to Jahn-Teller distortion of  $\text{Mn}^{3+}\text{O}_6$  octahedron,<sup>9-12</sup> the details on the topology of Mn-O sublattices and their association with lattice strains are still poorly understood regarding to electrochemical cycling performance of LMO.

Doping has been a key technique used to improve application properties of LMO. Shi et al. reported calculated intercalation voltages increasing along with the content of cationic dopants.<sup>14,15</sup> Singh et al. pointed out charge transfer from dopants to nearby oxygen and manganese ions in chromium and magnesium doped LMO.<sup>16</sup> Lee et al. found the degree of structural disorder around manganese ions in  $\text{LiAl}_{0.15}\text{Mn}_{1.85}\text{O}_4$  is lower than that of pristine

*a* Ningbo Institute of Material Technology & Engineering, Chinese Academy of Sciences, Ningbo 315201, China

*b* Wuhan University of Technology, Wuhan 430070, China

*c* Zhejiang WELLY Energy Corporation, Cixi 315301, China

*d* College of Mater. Sci. & Chem. Eng., Ningbo University, Ningbo 315211, China

*e* Ningbo Shijie New Energy Technology LLC, Cixi 315301, China

*f* Beijing University of Chemical Technology, Beijing 100029, China

See DOI: 10.1039/x0xx00000x

LMO.<sup>17</sup> Capsoni et al. found low ratio Al-doped LMO can decrease the transition temperature from cubic to orthorhombic phase,<sup>18</sup> and Yu et al. observed that Al-doping can improved cycling stability while reducing the capacity of LMO in the first several cycles.<sup>19</sup> Shen et al. suggested that cobalt dopant may help increase average valence state of manganese ions, reduce the concentration of trivalent manganese ions, therefore suppress the Jahn-Teller distortion in cobalt-doping LiMn<sub>2</sub>O<sub>4</sub>.<sup>11</sup> H. Şahan et al. and K. M. Shaju studied a wide range of doping schemes including Cobalt-doping and CoM (M=Ni, Zn, Cu, Al) dual-doping for improving Li diffusion and cycling stability of LMO.<sup>20, 21</sup> However, to our best knowledge, previous experimental exploration and theoretical calculation of doping schemes have paid little attention to their effects on cracking, and have ignored their connection to lattice strain. It remains unclear how local bonding characteristic impacts on the integrity of the overall lattice and what modification schemes may suppress the lattice strain introduced by Jahn-Teller distortion.

In this work, we combine first-principles calculations with experiments to reveal the correlation between alleviation of cracking and relieving of lattice distortion in LMO. Firstly, we present distinct cycling behaviours between undoped and Al/Co dual-doped LMO. This gives the first experimental evidence of the suppressing effect of Al/Co dual-doping on cracking in LMO particles. We employ first-principles calculations to compare LMO models with different doping schemes. First-principles calculated lattice changes and atomistic conformation are aligning to materials synthesized and their characterizations. The calculation finds that the networking of the ionic, i.e., the distribution of mixing valences Mn<sup>3+</sup> and Mn<sup>4+</sup>, plays a key role in the strain building and relieving among Mn-O sublattices, Al/Co dual-doping are correlated to a lattice with strain well-relieved, in contrast to undoped and other single cationic doping, in which lattice distortion cannot be compensated well between Mn<sup>3+</sup>O and Mn<sup>4+</sup>O sublattices. This study may offer not only new insights on cationic doping in spinel LMO as a special, but also new synergistic approach to prevent the cracks for other electrode materials in general.

## 2 Experimental procedures

Samples of cationic doped LiMn<sub>2</sub>O<sub>4</sub> were prepared by a solid state reaction technique. The raw materials were Li<sub>2</sub>CO<sub>3</sub> (Tianqi, 99%), MnO<sub>2</sub> (Aldrich, 99%) and corresponding dopants Al<sub>2</sub>O<sub>3</sub> (Aldrich, 99.999%), and Co<sub>3</sub>O<sub>4</sub> (Aldrich, 99.999%). The materials were ball milled for 2h and dry in vacuum at 90°C for 6h. Then, the dried mixture was grinded and sintered at 350°C for 1h, 500°C for 2h and 660°C for 3h, successively. Finally, the mixture was grinded again and sintered at 860°C for 15h. Details of materials synthesis may be published elsewhere.

Crystal structure of the prepared samples was evaluated by X-ray diffraction (XRD, XRD-6100, Shimadzu) using Cu-K $\alpha$  radiation ( $\lambda = 1.5418\text{\AA}$ ). The morphology of materials was studied by scanning electron microscope (SEM, FEI, QUANTA 250 FEG). The elemental composition and distribution were examined by energy dispersive X-ray spectroscopy (EDS). The valence state of each element was analysed by X-ray photoelectron spectrometer (XPS, PHI 3056) with

an Mg K $\alpha$  radiation at a constant power of 100 W (15 kV and 6.67 mA).

The working electrodes were fabricated by mixing 85:10:5 (w/w/w) ratio of active material, super P carbon and polyvinylidene fluoride (PVDF), respectively, using N-Methyl-pyrrolidone (NMP) as the solvent. The mix slurry was coated on aluminium foil current collector and dried in vacuum at 120°C for 12h. The electrode foils were subsequently pressed and punched into circular discs. CR2032 coin cells were assembled with prepared electrodes as the cathode, lithium foil as the anode, a micro-porous membrane (Celgard 2550) as the separator and a few drops of electrolyte (1M LiPF<sub>6</sub> dissolved in EC/DMC with the volume ratio of 1:1). The assembly of coin cells was completed in an Ar-filled M-Braun glove box. The electrochemical performance of cells were tested on a battery tester of Land 2001A (Wuhan, China) in voltage range of 3.0-4.3V (vs. Li<sup>+</sup>/Li) at the rate of 1C (148mAh/g) at 25°C.

## 3 Computational details

All first-principles calculations in the present work were carried out in the generalized gradient approximation (GGA) suggested by Perdew, Burke and Ernzerhof (PBE) within density functional theory (DFT), as implemented in the Vienna Ab-initio Simulation Package (VASP).<sup>22-24</sup> The Hubbard parameter correction (GGA+U) is adopted to address the strong onsite Coulomb interaction for manganese ions and the Hubbard correlation parameter was set as  $U=4.84$  eV, following Xu et al.<sup>25</sup> According to the study of Wang et al., the Hubbard correction was not applied for cobalt ions.<sup>26</sup> The ion-electron interaction is described by the projector augmented wave method (PAW).<sup>27, 28</sup> One-, six-, four-, seven- and nine-valence electrons are considered explicitly for Li ( $2s^1$ ), O ( $2s^2 2p^4$ ), Al ( $3s^2 3p^1$ ), Mn ( $3d^5 4s^2$ ) and Co ( $3d^7 4s^2$ ), respectively. Integrations over Brillouin zone were carried out using Monkhorst-Pack special k point mesh of  $4\times 4\times 4$  for undoped and cationic doping LMO.<sup>29</sup> A cutoff energy of 500 eV was used for the plane wave expansion of wave functions. Structural relaxations were performed with the total energy converged to  $10^{-4}$  eV. All forces acting on ions were smaller than  $0.01$  eV  $\text{\AA}^{-1}$ . The ferromagnetic configurations were employed to calculate undoped and cationic doping LMO.

Spinel LMO crystallizes in  $Fd\bar{3}m$  cubic structure with oxygen ions on 32e sites forming a close packed FCC lattice, in which manganese and lithium ions occupy on 16d octahedral sites and 8a tetrahedral sites, respectively.<sup>30</sup> In single doping scheme, all 16d sites are equivalent for either one aluminium or one cobalt occupation in LMO unit cells. Two representative non-equivalent configurations, i.e. the shortest and longest distance between the two different dopants, aluminium and cobalt atoms, were investigated to gain atomistic understanding of the electrochemical performances. Through total energy calculation, it was found that two dopants prefer to separate as far as possible, indicating dopants intend to disperse in LMO lattice.

## 4 Results and Discussion

### 4.1 Experiment Analysis

The EDS measurement presented in Figure 1(a, b) and Table 1 suggests the chemical formula is  $\text{LiMn}_{1.927}\text{Al}_{0.056}\text{Co}_{0.017}\text{O}_4$  that is close to the designed mole ratio of Mn: Al: Co as 1: 0.02: 0.008. Due to the existing of conductive tapes, the content of carbon and oxygen is not accurate. The powder XRD patterns of LMO and LMO-Al/Co are compared in Figure 2(a), indicating both diffraction peaks can all be indexed on the basis of a cubic lattice with a space group  $Fd\bar{3}m$  (JCPDS NO.35-0782), and both compounds are in single phase with good crystallites. The peaks of LMO-Al/Co are sharper than the undoped LMO, indicating better crystallinity with larger particle size for LMO-Al/Co. The influence of cationic doping in the lattice can be compared from the relative shifts of peaks. As shown in Figure 2(b), with respect to undoped LMO (at  $43.96^\circ$ ), the peaks of (4 0 0) shift slightly but observably to  $43.98^\circ$ ,  $44.00^\circ$  and  $44.02^\circ$  for Al, Co and Al/Co doped LMO, respectively, indicating cations doped in the lattice. Lattice parameters obtained by Rietveld refinement showed the  $a$  value of LMO-Al/Co is slightly decreased to  $8.2182 \text{ \AA}$  from  $8.2303$  of LMO, correlating to a small cell volume shrinking from  $557.5$  to  $555.0 \text{ \AA}^3$ .

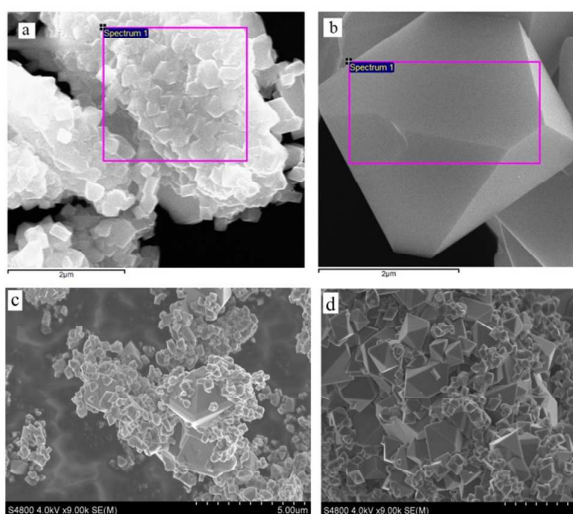


Figure 1 The SEM images for EDS of LMO (a) and LMO-Al/Co (b). The area inside the purple box was analyzed by EDS. The SEM images of LMO (c) and LMO-Al/Co (d) with larger multiple.

The difference between undoped LMO and LMO-Al/Co is distinguishable easily in particle size and morphology. Figure 1(c) and 1(d) compares the average size of pristine LMO and LMO-Al/Co particles,  $200\text{nm}$  vs.  $2.5\mu\text{m}$ , respectively. Particles around  $2.5\text{-}3\mu\text{m}$  can also be observed in undoped LMO. Figure 1(c, d) indicates that most LMO particles have irregular shapes, in contrast to the smooth surface and clear edge exhibiting almost in all the particles of LMO-Al/Co, which is consistent with the typical shape of a symmetrical cubic lattice formed by octahedral metal oxide units ( $\text{TO}_6$ ). It has been suggested that regular octahedral  $\text{TO}_6$  structure may significantly improve the electrochemical performance of LMO.<sup>31</sup> Therefore, Al/Co dual-doping may be an effective means to control

the particle morphology, being a favourable factor to improve the performance of LMO.

Table 1 The EDS analysis of LMO and LMO-Al/Co at room temperature

Element	LMO-Al/Co		LMO	
	Weight%	Atomic%	Weight%	Atomic%
C K	0.12	0.24	0.15	0.33
O K	50.21	77.21	44.98	73.54
Al K	0.69	0.63		
Mn K	48.54	21.74	54.87	26.13
Co K	0.45	0.19		
Totals	100.00		100.00	

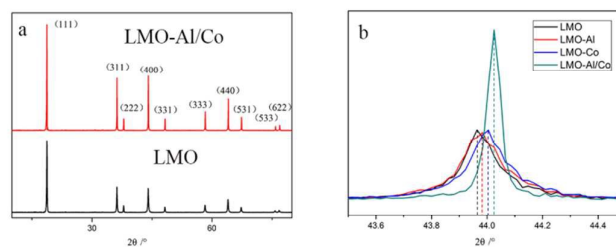


Figure 2 The powder XRD patterns of LMO and LMO-Al/Co at room temperature (a). And the XRD spectra around p peak (4 0 0) for undoped and different cationic doped LMOs (b).

The electrochemical performance of LMO and LMO-Al/Co are compared in Figure 3. Figure 3(a) shows the initial charge and discharge curves of LMO and LMO-Al/Co at a current rate of 1C at room temperature. The shape of the two curves is very similar, indicating Al/Co dual-doping does not change the electrochemical characters regarding to lithium ion occupation in and deintercalation from the lattice of LMO. The initial charge/discharge capacity of LMO and LMO-Al/Co are  $123.1/110.3$  and  $119.7/107.3\text{mAh/g}$ , respectively. The Columbic efficiencies are almost the same at 89.6%. The smaller stoichiometric ratio of Mn ion in LMO-Al/Co is the cause of slight lower capacity in the first cycle.

The cycling performances of LMO and LMO-Al/Co at different rate are evaluated in voltage window between 3.0V and 4.3V in Figure 3(b). LMO shows a rapid decreasing in discharging capacities from  $110.3\text{mAh/g}$  to  $84\text{mAh/g}$  at 1C,  $106.8\text{mAh/g}$  to  $78.3\text{mAh/g}$  at 2C and  $103.2\text{mAh/g}$  to  $66.2\text{mAh/g}$  at 5C after 350 cycles, giving a capacity retention rate 76.2%, 73.3% and 64.1%, respectively, in contrast to the retention rate 84.1%, 82.9% and 75.1% of LMO-Al/Co from  $107.3\text{mAh/g}$  to  $90.2\text{mAh/g}$  at 1C,  $105.4\text{mAh/g}$  to  $87.4\text{mAh/g}$  at 2C and  $98.6\text{mAh/g}$  to  $74\text{mAh/g}$  at 5C after 350 cycles, respectively. The difference in retention rates increases with discharging rates. This result confirms that Al/Co dual-doping

## ARTICLE

indeed improve the long-term cycling stability of LMO, especially at higher discharging rates.

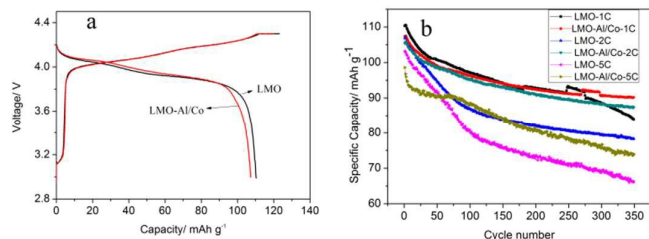


Figure 3 The initial charge/ discharge curves of LMO and LMO-Al/Co at 1C at room temperature (a) and the long-term cycling performances of LMO and LMO-Al/Co at 1C, 2C and 5C (b).

The cycling performance of LMO and LMO-Al/Co at 55°C is also compared in Figure 4. It shows that LMO has larger polarization between charging and discharging than LMO-Al/Co. The difference of discharge capacity retention becomes very obviously after 50 cycles. The discharging capacity of undoped LMO decays from 109.6mAh/g to 60.2mAh/g after 180 cycles at 2C and from 100.2mAh/g to 54.9mAh/g at 5C. LMO-Al/Co demonstrates 22% and 9% higher retention rates than LMO at 2C and 5C, respectively.

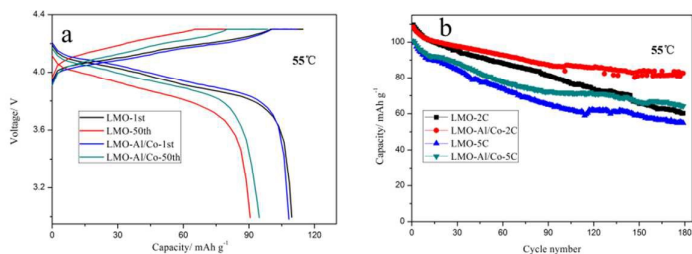


Figure 4 The initial charge/ discharge curves of LMO and LMO-Al/Co at 2C at 55°C (a) and the long-term cycling performances of LMO and LMO-Al/Co at 2C and 5C (b).

More interesting observation comes from the comparison of particle morphology after cycling. Figure 5 compares the surface morphology of LMO and LMO-Al/Co after 50 cycling at 2C. Figure 5(a1), (a2), (a3) and (a4) are the large particle selected randomly from Figure 5(a), Figure 5(b1), (b2), (b3) and (b4) are the large particle selected randomly from Figure 5(b). Figure 5(a1-a4) and Figure 5(b1-b4) demonstrate very distinct difference. Obvious cracks have appeared on LMO large particle surface (~2.5 $\mu$ m) but only very little traces on LMO-Al/Co particle surface at the same size and even larger particle of about 4 $\mu$ m. The cracking inclination becomes much more obvious after 350 cycling. After examining the electrodes carefully, we found there are no LMO particles bigger than 4  $\mu$ m and almost all particles around 3 $\mu$ m have fractures, while large Al/Co LMO particles of 4 $\mu$ m is still clean after long-term cycling and the trace on large particle of LMO-Al/Co remains tiny, c.f., Figure 6 (a-b). This is against the opinion on the general relation between cracking tendency and particle size, which would predict larger Al/Co LMO to be much easier to pulverize than does undoped LMO in cycling. From the point of battery application, the cracking inhibition is a highly preferred material property, which assures the

intact electronic and ionic channels of the electrodes in long-term battery uses.

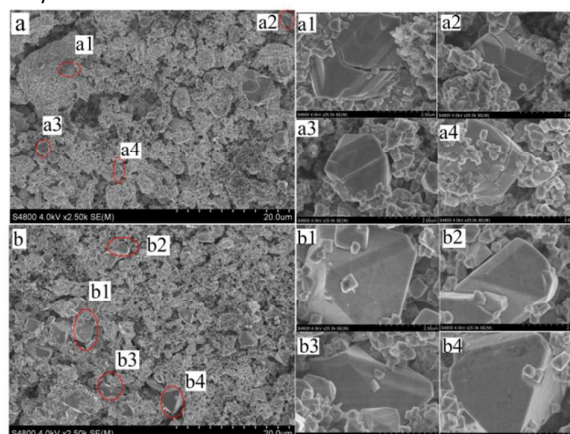


Figure 5 The SEM images of LMO (a) and LMO-Al/Co (b) after 50 cycling at 2C. (a1), (a2), (a3) and (a4) are the enlarged views of selected particles in Figure 5(a). (b1), (b2), (b3) and (b4) are the enlarged views of selected particles in Figure 5(b).

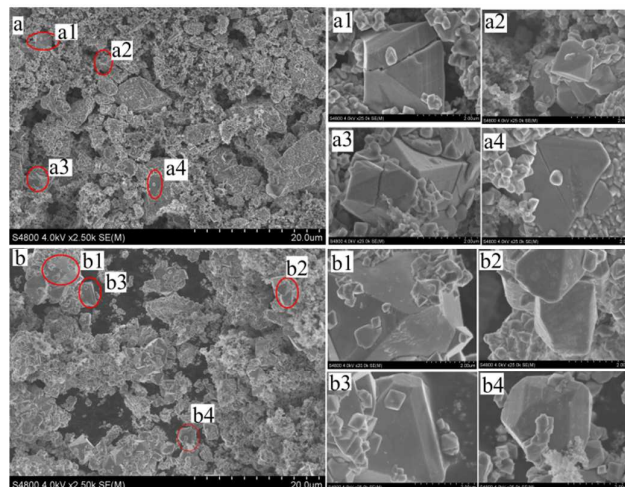


Figure 6 The SEM images of LMO (a) and LMO-Al/Co (b) after 350 cycling at 2C. (a1), (a2), (a3) and (a4) are the enlarged views of selected particles in Figure 6(a). (b1), (b2), (b3) and (b4) are the enlarged view of selected particles in Figure 6(b).

#### 4.2 Theoretical analysis

Our experimental finding indicates that particle size is not the sole factor to determine the particle cracking. The same charging/discharging character showed in Fig. 3a allows us to use the same first-principles approach to compare the local bonding characteristic in undoped and doped materials, from lithiated to delithiated phases, model by model at the same accuracy. The distinct cracking tendency between undoped and Al/Co dual-doped LMO is attributed to the different lattice strain mechanism between  $\text{Li}^+$  intercalation and deintercalation in LMO (MO) and LMO-Al/Co (MO-Al/Co). Table 2 gives the first clear comparison of calculated lattices among undoped, single (Al or Co)-doped, dual (Al/Co)-doped LMO, MO and MO-Al/Co. While experimental XRD reports a

cubic lattice with the length of 8.248 Å for spinel LMO,<sup>32</sup> our first-principles calculations at GGA+U level indicates the lattice distorted from cubic to orthogonal for LMO, agreeing with the trend reported by Ouyang et al. and Gao et al.<sup>33, 34</sup> When one Mn ion is substituted by Al or Co in the cubic lattice, it is found the axes variation is weakened in both Al and Co single doping. When one Al and Co ions simultaneously substitute two Mn ions in the cube lattice, there are two representative, non-equivalent cation doping configurations. The major difference between these two configurations is the separation distance between Al and Co, which are 5.85Å and 2.92Å, respectively. The total energy of the former one is about 0.1 eV per pair lower than the other one, indicating that Al and Co ions prefer scattered distribution on doping sites. The lattice of this model is given in Table 2 and is taken as the model for the dual (Al/Co)-doped LMO. It is worth to note that this model has the smallest axis distortion  $\Delta L$  (%) among all our first-principles models. It is close to cubic lattice, this may account for the big, symmetric growth of LMO-Al/Co materials.

Table 2 The calculated lattice parameters for undoped LMO, single Al-, Co-doped, dual Al/Co-doped LMO, MO and MO-Al/Co. The label  $\Delta V$  represents volume shrinkage,  $\Delta a$ ,  $\Delta b$ ,  $\Delta c$  are axis shrinkages by delithiation, and  $\Delta L$  is discrepancy between the longest and shortest axis lengths.

Materials	a (Å) ( $\Delta a$ )	b (Å) ( $\Delta b$ )	c (Å) ( $\Delta c$ )	V (Å <sup>3</sup> ) ( $\Delta V$ )	$\Delta L$ (%)
LiMn <sub>2</sub> O <sub>4</sub>	8.234	8.768	8.234	594.11	6.48
Mn <sub>2</sub> O <sub>4</sub> (MO)	8.265 (-0.4%)	8.266 (5.7%)	8.265 (-0.4%)	564.67 (5.2%)	-
LiAl <sub>0.125</sub> Co <sub>0.125</sub> Mn <sub>1.75</sub> O <sub>4</sub>	8.373	8.350	8.307	580.68	0.79
Al <sub>0.125</sub> Co <sub>0.125</sub> Mn <sub>1.75</sub> O <sub>4</sub> (MO-Al/Co)	8.253 (1.4%)	8.251 (1.4%)	8.261 (0.6%)	562.57 (3.2%)	-
LiAl <sub>0.125</sub> Mn <sub>1.875</sub> O <sub>4</sub>	8.288	8.575	8.258	586.85	3.84
LiCo <sub>0.125</sub> Mn <sub>1.875</sub> O <sub>4</sub>	8.683	8.221	8.228	587.29	5.62

Both lattices of the delithiated phase of LMO and LMO-Al/Co are close to cubic. However, the lithiated phase of the former is tetragonal with **b** axis about 6.48% longer than **a**, while the latter is close to cubic. It indicates that undoped and Al/Co doped materials undergo very different lattice changes by delithiation. After delithiation, besides obvious lattice transformation from tetragonal to cubic for undoped LMO, seen in Table 2, only one lattice axis shrinks about 5.7%, while the other two expands a little (smaller than 0.4%), and the cell volume shrinks along the direction of the long axis to about 5%. In dual-doped Al/Co, the shrinkages of the lattice axes are almost uniformly and not larger than 1.4%, and the shrinkage of the cell volume is almost symmetrical and reduces to 3.1%. The smaller and much more symmetrical shrinkage may reduce mismatch in the grain boundary between lithiated phase and delithiated phase of Al/Co dual-doped LMO. This may be a physical reason that undoped and dual-doped particles behave so differently in surface cracking after long-term cycling. This is beneficial to the diffusion of Li and decrease the building-up of Li on the two phase transition,<sup>35</sup> as well as reducing the strain in turn. The feature of calculated lattices in Table 2 also supports the argument of the partial suppression of two-phase formation which can be attributed to the improvement of Li<sup>+</sup> diffusion rate reported for Al/Co dual-doped LMO.<sup>21</sup> Therefore, the relieving of lattice mismatch in delithiation may be the physical root of the improved

cycling stability with high retention rates at higher discharging rates, and account for the disappearing of cracks on the surface of LMO-Al/Co particles after long-term cycles.

Detailed analysis on atomistic models relates the relieving of lattice strains to the network of octahedral metal oxide building-blocks (TO<sub>6</sub>). Al, Co and valence alternating Mn present different ionic bonding characteristic on the topology of Mn-O sublattices. Jahn-Teller distortion of Mn<sup>3+</sup>O<sub>6</sub> octahedron is the well-known mechanism to generate lattice deviation from cubic LMO. For undoped LMO, the short bond length between trivalent manganese and oxygen ions is about 1.975Å, and the long one is 2.210Å, consistent with the calculation of Nakayama.<sup>36</sup> In dual-doped Al/Co, the long and short bonds length of Mn<sup>3+</sup>O have changed to about 2.171Å and 1.956Å, respectively. The difference between the two kinds of bonds remains large. Figure 7 compares the overall atomistic conformation between undoped and dual-doped LMO. It can be seen that each Mn<sup>3+</sup>O<sub>6</sub> octahedron in LMO is a distorted polyhedron, seeing the thumbnail in Figure 7(a). In LMO-Al/Co, shown in Figure 7(b), the Mn-O bonds especially for the Mn<sup>3+</sup>O bonds have also distorted obviously with parts of the bonds in a wider angle, resulting in the asymmetry of each Mn<sup>3+</sup>O<sub>6</sub> octahedron. It indicates the distortion of the Mn<sup>3+</sup>O<sub>6</sub> octahedron in LMO-Al/Co is even larger than that in undoped LMO. Thus, the Jahn-Teller distortion exists in spinel LMOs with or without doping.

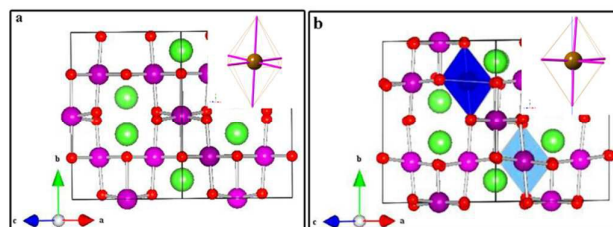


Figure 7 Schematic illustration of LMO (a) and LMO-Al/Co (b). The thumbnail is the bonding characteristic of Mn<sup>3+</sup>-O<sub>6</sub> building-blocks. Purple, green and red balls represent Mn, Li and O atoms respectively. The blue and sapphire polyhedrons represent Co-O<sub>6</sub> and Al-O<sub>6</sub> polyhedron

Our first-principles models indicate that while the distortion of building-blocks MnO<sub>6</sub> is the origin of lattice strains, the superposition of different distortions in the network, i.e., spatial distribution of Mn<sup>3+</sup>-O long bonds is the key factor to determine the lattice shape. Figure 8 show the spatial arrangement of Mn<sup>3+</sup>, Mn<sup>4+</sup>, Al and Co ions in the lattices. It can be seen from Figure 8(a) that the arrangement of Mn<sup>3+</sup> and Mn<sup>4+</sup> ions in undoped LMO are ordered well in clear layers of each kind of ion. Figure 8(c) plots all of the long bond orientation again in undoped LMO, which are nearly parallel to the same orientation along **b** axis; these results in building-up of high lattice strains as showed in the biggest axis variation (cf. Table 2). On the other hand, in LMO-Al/Co, Figure 8(b) shows that the Mn<sup>3+</sup> ions neighbour to Co have exchanged with the Mn<sup>4+</sup> ions of the adjacent layer. Figure 8(d) presents a 90° rotation for the long bond orientation of the exchanged Mn<sup>3+</sup>-O<sub>6</sub> and the one between the doped Co-O<sub>6</sub>. As a result of the random

orientation of  $\text{Mn}^{3+}\text{-O}_6$  long bonds, the axis variation has been significantly and effectively suppressed in LMO-Al/Co, and the lattice shape becomes almost cubic. This may be the local bonding characteristic leading to the big difference in particle size, morphology, and cracking tendency between LMO and LMO-Al/Co.

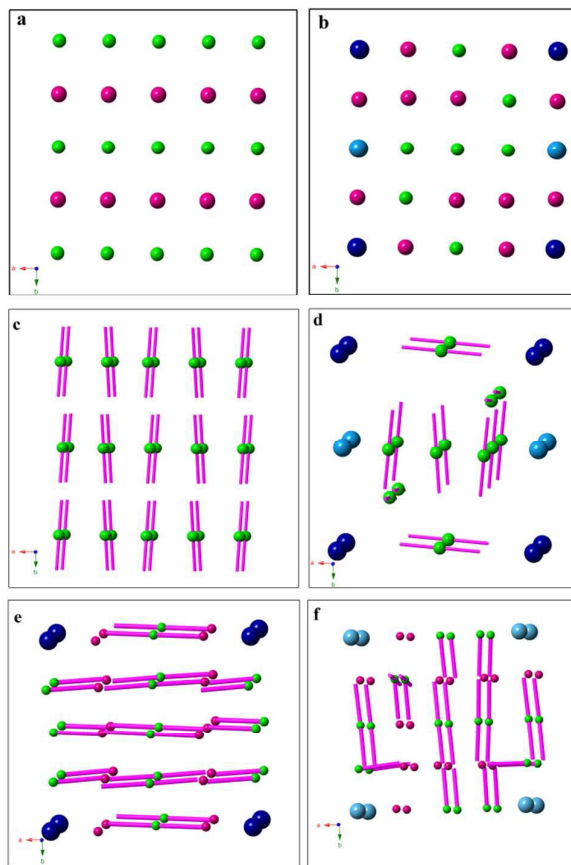


Figure 8 Schematic illustration of the spatial arrangement of the Mn ions for LMO (a) and LMO-Al/Co (b). The spatial arrangement of the long  $\text{Mn}^{3+}\text{-O}_6$  bonds for LMO (c) and LMO-Al/Co (d). The bonding characteristic of the longest  $\text{Mn}^{3+}\text{-O}_6$  bonds for LMO-Co (e) and LMO-Al (f). The red, green, blue and sapphire balls represent  $\text{Mn}^{4+}$ ,  $\text{Mn}^{3+}$ , Co and Al atoms respectively, the purple line represent the long  $\text{Mn}^{3+}\text{-O}_6$  bonds

The non-parallel orientation of the Jahn-Teller distorted  $\text{Mn}^{3+}\text{-O}_6$  is a synergetic effect of Al/Co dual doping. As showed in Table 2, single Al or Co doped LMO have different axis variation. Their bonding characteristic around manganese ions are sketched in Figure 8(d, e). It can be seen that while the distortion is only partially suppressed after aluminium or cobalt doped, their long bond orientation is very different. The latter one is the main factor to remove the building-up of lattice strains in Mn-O sublattices. Figure 8(d) displays that only Co doping cannot alter the orientation of the long  $\text{Mn}^{3+}\text{-O}_6$  bonds but shrink through the shorter Co-O bond. Figure 8(e) indicates Al doping will alter the orientation of

long  $\text{Mn}^{3+}\text{-O}_6$  bonds to a different direction. Therefore, both single cationic doping can compensation the distortion to some degree, agreeing with previous experimental results reported by He et al. and Shen et al.<sup>37, 38</sup> However, the Al/Co dual-doping combines advantage of both cationic influences, giving an effective relieving of lattice strains from Jahn-Teller distorted  $\text{Mn}^{3+}\text{-O}_6$ .

Electronic structures have not been affected by the dual-doping, indicating a good rate capability for doped LMO. The projected electron DOS of manganese ions in LMO and LMO-Al/Co are showed in Figure 9. They are consistent with the XPS results shown in Figure 9(c). According to the previous reports,<sup>39, 40</sup> the  $\text{Mn } 2\text{P}_{3/2}$  binding energies (BE) of  $\text{Mn}^{3+}$  and  $\text{Mn}^{4+}$  are observed at 641.9 and 643.2 eV. Figure 9(c) indicates the average oxidation state of Mn ion among LMO and LMO-Al/Co, of which the peak position is 642.4 eV and 642.6 eV, respectively, are the same. Nadine Treuil et al. reported that the valence state of Mn can be described as the composition of +3 and +4 from XPS fitting.<sup>41</sup> In LMO-Al/Co, there is no obvious change in binding energies of Mn ion, indicating no change in the valence state of Mn ion. The increase of 0.2 eV should be ascribed to the change of the ratio of  $\text{Mn}^{4+}/\text{Mn}^{3+}$ .<sup>41</sup> The result corresponds to the decrease of capacity in LMO-Al/Co at the first cycle. These confirm again the distortion of  $\text{Mn}^{3+}\text{-O}_6$  bond induced by Jahn-Teller distortion is still exist in the structure of LMO-Al/Co, which is compensated but not suppressed by the dual doping.

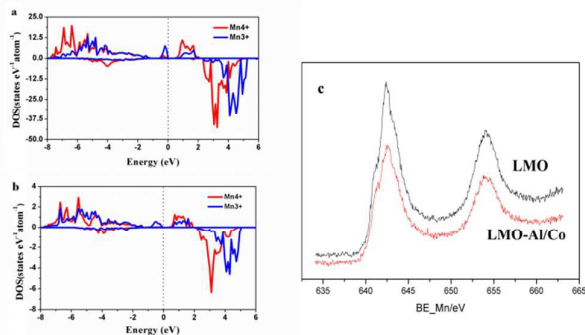


Figure 9 Projected electron density of state (DOS) of Mn 3d electrons in LMO (a), LMO-Al/Co (b) and the XPS pattern of the Mn ion of LMO and LMO-Al/Co (c)

## 5 Conclusions

Compared to undoped  $\text{LiMn}_2\text{O}_4$ , Al/Co dual-doped  $\text{LiMn}_2\text{O}_4$ , while bigger in average particle size, exhibits even better long-term cycling stability with capacity retention rate 84.1% after 350 cycles, 8% higher than undoped phase. The suppression of particle fracture by Al/Co dual-doping has been observed. This highly preferred material property has been attributed to the reduced boundary strain rooted in the lattice mismatch between lithiated and delithiated phase. It is worth to note that the dual-doping does not suppress the Jahn-Teller distortion of the building block  $\text{MnO}_6$ . Instead, it changes the distribution network of mixing valence Mn ions. The latter one is a much more important factor to release the

lattice strain, then to alleviate cracking on particle surface. The random distribution of Mn<sup>3+</sup>-O long bond orientation is a synergetic action of Al and Co. The symmetrical and small volumetric shrinkage by delithiation may account for the disappearance of cracks on the surface of Al/Co-LiMn<sub>2</sub>O<sub>4</sub> after 350 cycles, while some obvious cracks have developed in undoped LiMn<sub>2</sub>O<sub>4</sub> at similar particle size. That in turn improves the electrochemical cycling stabilities of LiMn<sub>2</sub>O<sub>4</sub>-Al/Co. One may expect that while bonding characteristic, which is the root of strain building-up at the lattice boundary, is materials dependent, there may exist a strategy to remove such strains by modifying the network of valence mixing elements using different bonding characteristic, such as in the case of Al/Co dual-doping. We are expecting that this kind of mechanism may be applicable to other electrode materials, both cathode and anode, in general.

### Corresponding Author

\*Correspondence: chenzhl@nimte.ac.cn (Zhenlian Chen),  
lijun@nimte.ac.cn (Jun Li)

### Acknowledgment

The authors acknowledge programs supported by the National Research program of China (2013AA050901), Public projects of Zhejiang Province (2015C31122), Zhejiang Natural Science Foundation (LY16B030007), Ningbo Natural Science Foundation (2015A610240), Zhejiang Province Key Science and Technology Innovation Team (2013PT16), and the National Young scholar Natural Science Foundation of China (201303235), the National Natural Science Foundation of China (11174301).

### References

1. L. Lu, X. Han, J. Li, J. Hua and M. Ouyang, *Journal of Power Sources*, 2013, **226**, 272-288.
2. M. S. Islam and C. A. Fisher, *Chemical Society reviews*, 2014, **43**, 185-204.
3. M. M. Thackeray, Wolverton, C. & Isaacs, E. D., *Energy & Environmental Science*, 2012, DOI: 10.1039/c2ee21892e, 7854.
4. R. Teki, M. K. Datta, R. Krishnan, T. C. Parker, T. M. Lu, P. N. Kumta and N. Koratkar, *Small*, 2009, **5**, 2236-2242.
5. W. Pu, X. He, J. Ren, C. Wan and C. Jiang, *Electrochimica Acta*, 2005, **50**, 4140-4145.
6. D. Wang, X. Wu, Z. Wang and L. Chen, *Journal of Power Sources*, 2005, **140**, 125-128.
7. Y.-I. J. Haifeng Wang, Biying Huang, Donald R. Sadoway, Yet-Ming Chiang, *Journal of Power Sources*, 1999, **81-82**, 594-598.
8. X. Hao, X. Lin, W. Lu and B. M. Bartlett, *ACS applied*

9. *materials & interfaces*, 2014, **6**, 10849-10857.
10. Doretta Capsoni, Marcella Bini, Gaetano Chiodelli, Piercarlo Mustarelli, Vincenzo Massarotti, Carlo B. Azzoni, Maria C. Mozzati and a. L. Linati, *J. Phys. Chem. B*, 2002, **106**, 7432-7438.
11. N. P. R. A. S. Wills, J. E. Greedan, *Chem. Mater*, 1999, **11**, 1510-1518.
12. C.-H. Shen, R. Gundakaram, R.-S. Liu and H.-S. Sheu, *Journal of the Chemical Society, Dalton Transactions*, 2001, DOI: 10.1039/b007120j, 37-40.
13. P. Piszora, W. Paszkowicz, C. Baehtz and E. Wolska, *Journal of Alloys and Compounds*, 2004, **382**, 119-122.
14. G. R. J. Rodríguez-Carvajal, C. Masquelier, and M. Hervieu, *PHYSICAL REVIEW LETTERS*, 1998, **81**, 21.
15. S. Shi, C. Ouyang, D.-s. Wang, L. Chen and X. Huang, *Solid State Communications*, 2003, **126**, 531-534.
16. S. Shi, D.-s. Wang, S. Meng, L. Chen and X. Huang, *Physical Review B*, 2003, **67**.
17. G. Singh, S. L. Gupta, R. Prasad, S. Auluck, R. Gupta and A. Sil, *Journal of Physics and Chemistry of Solids*, 2009, **70**, 1200-1206.
18. J. F. Lee, Y. W. Tsai, R. Santhanam, B. J. Hwang, M. H. Yang and D. G. Liu, *Journal Of Power Sources*, 2003, **119**, 721-726.
19. D. Capsoni, M. Bini, G. Chiodelli, V. Massarotti, P. Mustarelli, L. Linati, M. C. Mozzati and C. B. Azzoni, *Solid State Communications*, 2003, **126**, 169-174.
20. F.-D. Yu, Z.-B. Wang, F. Chen, J. Wu, X.-G. Zhang and D.-M. Gu, *Journal of Power Sources*, 2014, **262**, 104-111.
21. H. Şahan, H. Göktepe and Ş. Patat, *Inorganic Materials*, 2011, **44**, 420-425.
22. K. M. Shaju, G. V. Subba Rao and B. V. R. Chowdari, *Journal of Materials Chemistry*, 2003, **13**, 106-113.
23. G. Kresse and J. Hafner, *Physical Review B*, 1994, **49**, 14251-14269.
24. G. Kresse and J. Furthmüller, *Computational Materials Science*, 1996, **6**, 15-50.
25. G. Kresse and J. Furthmüller, *Physical Review B*, 1996, **54**, 11169.
26. B. Xu and S. Meng, *Journal Of Power Sources*, 2010, **195**, 4971-4976.
27. J. M. Wang, J. P. Hu, C. Y. Ouyang, S. Q. Shi and M. S. Lei, *Solid State Communications*, 2011, **151**, 234-237.
28. P. E. Blochl, *Physical Review B*, 1994, **50**, 17953-17979.
29. G. Kresse and D. Joubert, *Physical Review B*, 1999, **59**, 1758-1775.
30. H. J. Monkhorst and J. D. Pack, *Physical Review B*, 1976, **13**, 5188-5192.
31. N. Ishizawa and K. Tateishi, *J Ceram Soc Jpn*, 2009, **117**, 6-14.
32. G. Jin, H. Qiao, H. Xie, H. Wang, K. He, P. Liu, J. Chen, Y. Tang, S. Liu and C. Huang, *Electrochimica Acta*, 2014, **150**, 1-7.
33. J. Akimoto, Y. Takahashi, Y. Gotoh and S. Mizuta, *Chemistry of Materials*, 2000, **12**, 3246-3248.
34. C. Y. Ouyang, S. Q. Shi and M. S. Lei, *Journal Of Alloys And Compounds*, 2009, **474**, 370-374.
35. G. Tan-Hua, *Acta Phys. Sin*, 2012, **61**.
36. M. Y. Song, D. S. Ahn and H. R. Park, *Journal of Power Sources*, 1999, **83**, 57-60.
37. M. Nakayama and M. Nogami, *Solid State Communications*, 2010, **150**, 1329-1333.

## ARTICLE

Physical Chemistry Chemical Physics

37. B. L. He, W. J. Zhou, Y. Y. Liang, S. J. Bao and H. L. Li, *J Colloid Interface Sci*, 2006, **300**, 633-639.
38. C. Shen, R. Liu, R. Gundakaram, J. Chen, S. Huang, J. Chen and C. Wang, *Journal of Power Sources*, 2001, **102**, 21-28.
39. T. Qiu, J. Wang, Y. Lu and W. Yang, *Electrochimica Acta*, 2014, **147**, 626-635.
40. A. Bocquet, T. Mizokawa, T. Saitoh, H. Namatame and A. Fujimori, *Physical Review B*, 1992, **46**, 3771-3784.
41. Nadine Treuil, Christine Labruge `re, Michel Menetrier, Josik Portier, Guy Campet, Anne Deshayes, Jean-Claude Frison, Seong-Ju Hwang, Seung-Wan Song and J.-H. Choy, *J. Phys. Chem. B*, 1999, **103**, 2100-2106.